CrossMark

JFM RAPIDS
journals.cambridge.org/rapids

Assessing and improving the accuracy of synthetic turbulence generation

J. W. Patterson[1], **R. Balin**[1] **and K. E. Jansen**[1],†

[1]Department of Aerospace Engineering, University of Colorado, Boulder, CO 80309, USA

With the growing interest in scale-resolving simulations of spatially evolving boundary layers, synthetic turbulence generation (STG) has become a valuable tool for providing unsteady turbulent boundary conditions through a sum over a finite number of spatio-temporal Fourier modes with amplitude, direction and phase determined by a random number set. Recent developments of STG methods are designed to match target profiles for anisotropic and inhomogeneous Reynolds stresses. In this paper, it is shown that, for practical values of the number of modes, a given set of random numbers may produce Reynolds stress profiles that are 30 % off their target. To remedy this situation, the error in the STG stress prediction is decomposed into a steady-state bias and a purely unsteady part affecting the time convergence. Direct relationships between the random number vectors and both types of error are developed, allowing large collections of random number sets to be rapidly scanned and the best performers selected for a much improved agreement with the target. The process is verified for the inflow to a direct numerical simulation of a flat plate at $Re_\theta = 1000$. This paper demonstrates sufficient time convergence over a few flow-through times as well as a correction of the method's biases.

Key words: turbulence simulation, turbulent boundary layers

1. Introduction

The generation of unsteady and spatially varying velocity fluctuations is an essential component in the pursuit of efficient and accurate scale-resolving simulations of complex turbulent flows at increasingly larger Reynolds numbers. Whether the fluctuations are to be applied at the inflow of a computational domain or at the interface between scale-resolving and non-scale-resolving regions, it is imperative that they provide reproducible statistics that result in a short downstream development length. Various methods have been proposed to achieve this goal (Wu 2017), notably the use of precursor or parallel simulations, the recycling and rescaling of downstream instantaneous turbulence

† Email address for correspondence: kenneth.jansen@colorado.edu

(Lund, Wu & Squires 1998), the use of vortex generating devices near the surface, and artificial forcing through unsteady body force terms in the governing equations (Spille-Kohoff & Kaltenbach 2001). Synthetic turbulence generators add artificial velocity fluctuations to a known mean profile. Synthetic turbulence generation (STG) methods offer many advantages, such as computational efficiency and ease of implementation, and are extremely versatile since they require knowledge of local flow variables only.

The original idea for the STG method described herein is attributed to Kraichnan (1970), who represented an incompressible velocity field as a finite sum of spatio-temporal Fourier modes whose amplitude and phase are random. This methodology was then improved by Karweit *et al.* (1991) for incompressible isotropic turbulence. Their method produced turbulence fluctuations with zero mean and with the desired root mean square (r.m.s.) value. Béchara (1994) successfully used a similar definition of synthetic turbulence for noise modelling of free jet flows. Also of great significance is the work of Smirnov, Shi & Celik (2001), who developed a random flow generation procedure for turbulent shear flows with spatial inhomogeneity and anisotropy of the stresses. Their method takes as input the Reynolds stress tensor as well as the length and time scales of the turbulence (known *a priori* or available from the ongoing simulation) to produce more realistic velocity fluctuations that satisfy these inputs. Batten, Goldberg & Chakravarthy (2004) and Huang, Li & Wu (2010) improved upon these methods, allowing for a better representation of the anisotropy and the energy spectra of the synthetic turbulence, respectively. More recently, Adamian, Strelets & Travin (2011) and Shur *et al.* (2014) proposed a similar approach to develop anisotropic and inhomogeneous synthetic turbulence for aerodynamic applications, including noise measurements. Their formulation was specifically developed for hybrid Reynolds-averaged Navier–Stokes (RANS) and large-eddy simulation (LES) methods, but was shown in Spalart *et al.* (2017) and Balin, Jansen & Spalart (2020) to be effective for inflows to direct numerical simulations (DNS) as well.

The purpose of this work is to analyse and improve the convergence of the statistics of the velocity fluctuations produced by the STG formulation of Shur *et al.* (2014) to the desired local Reynolds stresses. The approximation of the infinite Fourier series with a finite number of wave modes as well as the finite integration time of the simulation lead to errors in the second-order statistics of the artificial turbulence that can negatively impact the development of realistic turbulence and the downstream flow. In this paper, the sources of these errors are clearly identified, and a strategy that allows for a much improved agreement with the target statistics is proposed. The temporal convergence rate to the target is also investigated. The efficacy of the STG method is therefore significantly enhanced, further expanding its range of applicability. For instance, in spatially developing flows where upstream history is critical (e.g. pressure gradient flows), errors in the shear stress can lead to realistic turbulence that does not match the target wall shear and result in poor predictions of the entire downstream flow. Having chosen a particular STG method to analyse, it is important to note that there are other competitive classes of STG such as the digital filtering method of Xie & Castro (2008). While some aspects are similar, and thus similar errors are likely, subtle differences in this approach and other STG methods will require further extensions to the analysis techniques described in this paper.

This paper is organized as follows. Section 2 is a review of the chosen STG method and a description of the bias and time convergence errors that come from the use of finite wave modes. Section 3 provides the analysis tools and understanding to rigorously assess these two errors. Section 4 verifies the improvement achieved on the inflow to a flat plate DNS and, finally, § 5 draws some conclusions.

2. Base synthetic turbulence generation

Following the STG method developed by Shur *et al.* (2014), the velocity at the domain inflow (or scale-resolving interface) is set to be the sum of a fluctuating and mean velocity field. The fluctuating part has the intent of prescribing an energy spectra that is realized in actual turbulence, a statistically stationary signal and a prescribed variance. The reader is referred to the original paper for more detail on the method's definitions, which are summarized as follows:

$$u'_i = a_{ij} 2\sqrt{\tfrac{3}{2}} \sum_{n=1}^{N} \sqrt{q^n} \sigma_j^n \cos(\kappa^n d_l^n \hat{x}_l + \psi^n), \qquad (2.1)$$

$$\left.\begin{aligned}
&\hat{x}_i \equiv \{(x_1 - U_0 t') \max(\kappa_e^{min}/\kappa^n, 0.1), x_2, x_3\}, \quad \sigma_j^n d_j^n = 0, \quad a_{ik} a_{jk} = R_{ij}, \\
&q^n \equiv \int_{\kappa^{n-1}}^{\kappa^n} E(\kappa^n)\, d\kappa \Big/ \int_0^\infty E(\kappa^n)\, d\kappa, \quad \sigma^n = \sigma^n(\theta^n, \phi^n), \\
&E(\kappa^n) = (\kappa^n/\kappa_e)^4 f_\eta f_{cut} [1 + 2.4(\kappa^n/\kappa_e)^2]^{-17/6}, \quad d_i^n = d_i^n(\theta^n, \phi^n, \eta^n).
\end{aligned}\right\} \qquad (2.2)$$

Einstein summation notation has been adopted when the contraction is between spatial dimensions (subscripts), while a sum is written for Fourier components (superscripts) since they are often repeated more than twice. The terms θ^n, ϕ^n, η^n and ψ^n are sets of random variables defined by their probability density functions and intervals: $f_\theta = \sin(\theta)/2$, $\theta \in [0, \pi]$; and $f_{\phi, \eta, \psi} = \pi/2$, $\{\phi, \eta, \psi\} \in [0, 2\pi]$. The two random sets of spherical angles θ^n and ϕ^n cause the set of unit vectors, σ_j^n, to be uniformly distributed on a unit sphere. Imposing a divergence-free velocity ($\sigma_j^n d_j^n = 0$ as verified in Smirnov *et al.* (2001)) together with the requirement that d_j^n be uniformly distributed on a unit sphere leaves d_j^n as a function of the dependent variables (θ, ϕ) of σ_j^n and the angle η in the plane normal to σ_j^n. The random angles, radial lengths and defined intensities are wave modes that have been mapped to wave space from a pseudo-isotropic turbulence via the spatial Fourier transform. Note that the definition of $\hat{x}_i$ provides a means to slide through this pseudo-turbulence domain by a spatial coordinate that progresses at the inflow bulk speed, U_0, naturally accounting for bulk convection. The second argument of the max is due to Shur (M. L. Shur, private communication 2020). Definitions for κ_e^{min}, f_η, f_{cut} and $k_e(x_i)$ match those given in Shur *et al.* (2014), where they were chosen to adjust the spectrum at each grid point on the inflow plane (eddy size and anisotropy) to accurately account for proximity to solid boundaries. Further, their approach of defining a_{ij} through a Cholesky decomposition of the Reynolds stress, R_{ij}, is adopted.

An increase in the number of wave modes directly corresponds to the number of realizations of this pseudo-turbulence flow in addition to the recovery of the correct normalized energy spectra or, in physical space, the autocorrelation functions (Béchara 1994). However, as all implementations of this STG boundary condition will use a finite number of wave modes and a finite number of time steps, what remains to be seen is, with N finite: (1) Does $\lim_{t \to \infty} \langle u'_i u'_j \rangle_t = R_{ij}$ and (2) does $\langle u'_i u'_j \rangle_t - \lim_{t \to \infty}[\langle u'_i u'_j \rangle_t]$ become acceptably small after a time t that is otherwise sufficient to converge statistics within the interior of the simulation domain (e.g. a small number of domain flow-through times)? Is there a dependence of getting one but not the other? Issue (1) will be referred to as the bias (infinite-time realized Reynolds stress) and (2) as time convergence. This work aims to provide independent measures of each that will enable improvements to both.

3. Analysis tools

The analysis begins with the intent of recognizing the mathematical expressions that separate the bias and time convergence accuracy of a particular random number set for N wave modes relative to the target covariance tensor of the velocity fluctuations:

$$\langle u'_l u'_m \rangle_t = a_{li} a_{mj} \langle v'_i v'_j \rangle_t, \tag{3.1}$$

where

$$\langle [f] \rangle_t \equiv \frac{1}{t} \int_0^t [f(t')] \mathrm{d}t', \quad \langle [f] \rangle_{tz} \equiv \frac{1}{tz} \int_0^z \int_0^t [f(t', z')] \, \mathrm{d}t' \, \mathrm{d}z'. \tag{3.2a,b}$$

Note from above that a_{ij} provides a scaling to the velocity fluctuations, leaving v_i to provide the instantaneous fluctuating direction, which follows from (3.1) and (2.1):

$$v'_i = 2\sqrt{\frac{3}{2}} \sum_{n=1}^{N} \sqrt{q^n} \sigma_i^n \cos(\kappa^n d_l^n \hat{x}_l + \psi^n). \tag{3.3}$$

This also makes it clear that the covariance of the fluctuation tensor, $\langle v'_i v'_j \rangle_t$, should converge to δ_{ij}, preferably within a time t that is comparable to the time required for the Reynolds stresses to converge in an experiment. In this paper, we will refer to such an averaging time as a physical averaging time due to it realistically reflecting the nature of the turbulence, while inputs that require substantially longer averaging time to converge the stresses are considered non-physical averaging times.

To better assess that, using (2.1), the covariance of the fluctuation tensor can be further decomposed into

$$\langle v'_i v'_j \rangle_t = \sum_{n=1}^{N} \sum_{p=1}^{N} \alpha_{ij}^{np} \beta^{np}, \tag{3.4}$$

$$\alpha_{ij}^{np} \equiv 6\sqrt{q^n q^p} \sigma_i^n \sigma_j^p, \quad \beta^{np} \equiv \frac{1}{t} \int_0^t \cos(\gamma^n t' + \hat{\psi}^n(\boldsymbol{x})) \cos(\gamma^p t' + \hat{\psi}^p(\boldsymbol{x})) \, \mathrm{d}t', \tag{3.5a,b}$$

$$\gamma^n = \frac{1}{t'} [\kappa^n d_i^n \hat{x}_i] \Big|_{x=0} = -U_0 d_1^n \max\left(2\kappa_{min}, \frac{\kappa^n}{10}\right), \quad \hat{\psi}^n = [\kappa^n d_i^n \hat{x}_i + \psi^n] \Big|_{t'=0}. \tag{3.6a,b}$$

Here, the fact that α_{ij}^{np} is independent of time has been exploited and the time integral has been propagated directly to β^{np}, which captures all of the temporal variation of (3.4) and ultimately (3.1). Analytically integrating (3.5a,b) yields

$$\beta^{np}(t) = \begin{cases} \dfrac{\sin((\gamma^n + \gamma^p)t + \hat{\psi}^n + \hat{\psi}^p)}{2(\gamma^n + \gamma^p)t} + \dfrac{\sin((\gamma^n - \gamma^p)t + \hat{\psi}^n - \hat{\psi}^p)}{2(\gamma^n - \gamma^p)t}, & n \neq p, \\[4mm] \dfrac{1}{2} + \dfrac{\sin(2(\gamma^n t + \hat{\psi}^n))}{4\gamma^n t}, & n = p. \end{cases} \tag{3.7}$$

The value of this split is made more clear by considering the infinite-time limit of (3.7):

$$\lim_{t \to \infty} \beta^{np} = \tfrac{1}{2}\delta^{np}. \tag{3.8}$$

With these definitions, the previously stated two objectives (the bias and time convergence of this method) can now be analysed by independently inspecting $\sum_n \sum_p \alpha^{np} \delta^{np}/2 = \sum_n \alpha^{nn}/2$ (the infinite-time value of (3.4)) and $\beta^{np}(t)$. From the former, it is clear that σ_i^n influences the infinite-time bias with no influence from d_i^n. Conversely, the latter indicates that d_i^n, and specifically d_1^n, influences the temporal convergence with no influence from σ_i^n. This point is made more clear in subsequent sections but, for now, it is observed that the sine terms of (3.7) are bounded by 1 but the denominators beneath them are influenced by the size (for $n = p$) and closeness of magnitude (for $n \neq p$) of γ^n, which is linear in d_1^n. The restriction that $d_i^n \sigma_i^n = 0$ for each n means that the prescriptions of α_{ij}^{np} and β^{np}, while separable, are not completely independent of each other.

It is understood (Kraichnan 1970) that, as the number of realizations (or equivalently number of wave modes N) increases, the covariance of the fluctuation tensor in (3.1) converges to δ_{ij}. Infinite or even very large N is intractable for practical numerical simulations for the obvious reason of the cost of evaluating (2.1). In the sections that follow, N will be treated as fixed to $O(500)$. It will be shown that this N is large enough to allow acceptably low bias error and to allow time convergence of the STG fluctuations to mimic the physical time needed for time convergence of turbulence statistics within the interior of the simulation. This ensures that the unsteady inflow or scale-resolving interface does not artificially raise the number of time steps required by the simulation.

3.1. *Error measurements*

Below are measures of error for any given random number choice (through (3.5*a,b*)):

$$e_{ij}^{\alpha} = \alpha_{ij}^{nn} \tfrac{1}{2} - \delta_{ij}, \tag{3.9}$$

$$e_{ij}^{R_b} = a_{il}a_{jm}e_{lm}^{\alpha}, \tag{3.10}$$

$$e_t^{np} = \langle \beta^{np} \rangle_t - \tfrac{1}{2}\delta^{np}, \tag{3.11}$$

$$e_{ij}^{R_t} = a_{il}a_{jm}\langle v_j v_m \rangle_t - \langle u_i' u_j' \rangle_{t \to \infty}, \tag{3.12}$$

$$e_{ij}^{R_t} \leqq \frac{24}{t} a_{il}a_{jm} \sum_{n=1}^{N} \sum_{p=1}^{N} \sigma_l^n \sigma_m^p \left\{ \begin{array}{ll} \dfrac{cq^n}{|\gamma^n|}, & n = p, \\[2mm] \dfrac{c\sqrt{q^n q^p}}{||\gamma^n| - |\gamma^p||}, & n \neq p, \end{array} \right\} \tag{3.13}$$

$$e_b^R = e_{ij}^{R_b} w_{jl} e_{li}^{R_b}, \quad e_t^R = e_{ij}^{R_t} w_{jl} e_{li}^{R_t}. \tag{3.14a,b}$$

These error measures will be explained in detail in the following two subsections.

3.2. *Bias considerations*

With a modest $N = O(500)$ spherically uniform random wave mode application, the bias in inflow spatio-temporal covariances has been observed to be up to 30 % off the target.

The fluctuation bias error (3.9) depends upon a wave mode contraction of (3.5*a*,*b*), which exposes the dependence not only on σ_i^n but also on the normalized energy of mode n, q^n, which is a function of position. Such an error measure neglects that the a_{ij} is also a function of position and it further couples fluctuation errors. With the exception of a_{11}, the scaling is increasingly dependent on the accuracy of the other entries:

$$a_{ij}(x_l) = \begin{bmatrix} \sqrt{R_{11}(x_l)} & 0 & 0 \\ R_{21}(x_l)/a_{11} & \sqrt{R_{22}(x_l) - a_{21}^2} & 0 \\ R_{31}(x_l)/a_{11} & (R_{32}(x_l) - a_{21}a_{31})/a_{22} & \sqrt{R_{33}(x_l) - a_{31}^2 - a_{32}^2} \end{bmatrix}. \quad (3.15)$$

Take, for example, a non-zero fluctuation bias error in (3.9) and $R_{11} = R_{22}$. Then using (3.10) the percentage error on R_{12} is

$$e_{12}^{R_b}/R_{21} = a_{11}a_{21}e_{11}^\alpha/R_{21} + a_{11}a_{22}e_{12}^\alpha/R_{21} = e_{11}^\alpha + e_{12}^\alpha\sqrt{(R_{11}/R_{21})^2 - 1}. \quad (3.16)$$

This is to say that the percentage difference of bias is proportional not only to the convergence of the isotropic fluctuation tensor but also to the ratio of the target stresses. Generally, the percentage error increases in growing row and column with any anisotropic stress and non-zero total fluctuation error. This propagation of error is directly accounted for in (3.10). However, to further compensate for this error amplification, the first equation in (3.14*a*,*b*) contracts the elements of the stress tensor error with a weight tensor, w_{jl}, which allows more weight to be given to stress components that are viewed as more important (e.g. shear stress) to accurately simulate the inflow, and to stress components that would otherwise accumulate more error.

With a precise measure of the bias error in hand, its inputs can be determined. As described in Shur *et al.* (2014), the target stresses are assumed known, potentially from an upstream RANS or other experiment. The normalized spectra are also assumed to be determined as a function of the inflow plane mesh resolution (which sets κ_{max}), the domain width (which sets κ_{min}), the wave mode spacing κ^n (with κ^n grown geometrically from κ^{min} to κ^{max} at a rate of $\approx 1\%$), and the energy spectrum E given as part of (2.1). This leaves only the four random angles needed to define σ_j^n, d_j^n and ψ^n. It is indeed these random number choices that will determine the bias of this procedure. Taking the first set of random angles could lead to an acceptable bias but, more than likely, will lead to a poor bias relative to what could be achieved by considering alternatives. Equations (3.14*a*,*b*) provide a means to evaluate the quality of a given random number set at any location on the inflow plane. That information can be used to find the worst location or can be averaged in space. Furthermore, the error can be studied over a variety of time intervals. Specific choices are discussed in § 4. Whatever the choice, by repeating this measurement for a large number of random number sets allows quick determination of the sets resulting in lowest bias, which is a key aspect of accurately matching the target inflow stress statistics.

3.3. *Time convergence considerations*

Slow time convergence of the second-order moments (stresses) provided by the STG inflow fluctuations artificially slows the convergence of all interior flow quantities – a situation best avoided. Two pathologies related to d_j^n vectors have been identified that limit the ability of the method to converge in a physically realistic amount of time. Examining (3.7)

for β_{np}, it may be observed that the rate of convergence in time agrees with the design constraint developed by Kraichnan (1970) of a realistic autocorrelation function. However, the amount of time that it takes to converge is dependent upon the pathologically poor mode pairs. Notice that γ^n adopts the units of inverse time. This exposes that when either $|\gamma^n|$ or $||\gamma^n| - |\gamma^p||$ is small then the time to converge is large. Since the only non-deterministic variable in γ^n from (3.6a,b) is d_1^n, the restriction upon γ^n is a restriction on d_1^n.

Equation (3.11) provides a direct measure of the error in the time term but, since it lacks weighting of the normalized spectra, it cannot distinguish between slow convergence of important high-energy modes and less impactful very low-energy modes. To rectify that, and to account for the aforementioned redistribution of the error through the a_{ij} coefficients, this error is scaled by the normalized energy of mode n, q^n, (borrowed from the α_{ij}^{np} term) and propagated to the Reynolds stress in (3.12). Unlike the bias considered in the previous subsection, which removed all temporal convergence error by using the infinite-time (exact) result of β^{np} in (3.9), for a given random number set, it is impossible to fully isolate temporal convergence error from bias. However, once bias has been minimized over a large sample of random number choices to find a set of σ_j^n vectors, d_j^n vectors can be evaluated against the error measure provided by (3.13) to evaluate their propensity to slow down temporal convergence. Note that c in (3.13) is an $O(1)$ constant. Again, this provides a very low-cost means to evaluate a large sample of random number sets and choose one with an acceptable convergence of the velocity covariance tensor (Reynolds stress). As with the bias, time convergence will in general be uneven by components and thus the second part of (3.14a,b) provides a means to apply higher weights to components that are deemed more important or more vulnerable to propagation error.

3.4. *Sequential choosing*

The above subsections outline a procedure to choose the two random number sets, θ^n and ϕ^n, that produce a σ_i^n that minimizes bias (infinite-time deviation from the target stress). Subsequently, the sequential choosing method then chooses a third random number set η^n that, with σ_i^n, produces the d_j^n vectors. The first component d_1^n defines γ^n that must be neither too small nor too close in absolute magnitude to all other γ^p to avoid slow time convergence in the significant energy modes as measured by (3.13). Note also that, all else the same, the phase angle ψ^n does alter early-time convergence; however, it can be made negligible to the other pathologies with longer time averaging.

Initial efforts to apply this approach provided substantial improvement of both bias and temporal convergence rate by considering only 10 000 sets of random numbers that were re-seeded at each draw. Larger collections of random number sets provided some improvement, but diminishing returns were observed. Reversing the order amounts to first finding the d_j^n (using two random spherical angles) that provides improvement to time convergence and then using the remaining random angle to find the σ_i^n that reduces bias. This reversed the situation; improved temporal convergence but bias was higher than when σ_i^n was chosen first.

3.5. *Alternative choosing*

The above analysis motivated the consideration of alternative procedures for the selection of the random variables. The first alternative considered was to choose all four random number sets and take a weighted combination of both errors given by (3.14a,b) so as to

obtain a combined measure of bias and temporal convergence. As might be expected, this produced more balanced results that were each better than the second choice but substantially less improved than when they were the first in the sequential choosing approach.

The second alternative considered follows the σ-first sequential choice process (fully random and uniformly distributed procedure selecting for low bias) but then allows the η^n to be chosen one at a time (not random) such that the resulting d_i^n minimize the pathologies associated with time convergence (i.e. (3.14a,b)). While this approach clearly tampers with the fundamental assumptions of the method (fully random), it is asserted that an 'intelligent design' of prescribing d_i^n vectors to minimize this pathology could be fruitful in cases where fully random numbers lead to inflow stress convergence that is slower than that typically observed on the interior of the computational domain.

The method of choosing d_i^n vectors is systematic according to the two pathologies from (3.13). From a set of N σ_i^n wave modes, it starts with lowest wavenumber ($n = 1$). The only pathology that exists for the first wave mode is the diagonal pathology. The plane that is perpendicular to σ_i^1 intersected with the unit sphere creates a circle that spans the admissible d_i^1. Given two unit vectors in that plane, η provides a combination to define d_i^n. There are exactly two η angles that minimize the diagonal mode pathology (except when $\sigma_1^1 = 1$, which must be forbidden due to it yielding $\gamma^n = 0$, which would require infinite time to converge). The subsequent wave mode choices, l, are then influenced by one diagonal pathology and $l - 1$ cross wave pathologies. These are not weighted equally as determined by the specific wavemode's normalized energy q^p for $p \le l$. By the construction of the pathologies, there will always be at least two optimal η that have the same pathological impact. From mode to mode the method randomly chooses between these two η to more uniformly distribute d_j^n on the unit sphere.

4. Verification and results

As a test of the developments discussed above, a zero-pressure-gradient flow over a flat plate was considered. At the location of the inlet, the momentum thickness Reynolds number is $Re_\theta = 1000$. The wall-normal spacing is typical of DNS with the first point located at $y^+ = 0.1$ growing geometrically at a rate of 1.05 until reaching approximately $y^+ = 10$, after which it is held at this spacing until $y = 1.2\delta_0$, where δ_0 is the inflow boundary layer thickness. A structured spanwise spacing of $\Delta_z^+ = 6$ is maintained throughout the inflow. The streamwise spacing influences the spectra (Shur *et al.* 2014) and the time step and thus $\Delta_x^+ = 10$ leads to a time step of $\Delta_t = 3 \times 10^{-6}$, which corresponds to a non-dimensional time step of $\Delta_t^+ = 0.2$. When studying the quality of the STG inflow on a flat plate, a domain length of $8\pi\delta_0$ is adequate since the domain only needs to be long enough for the inflow to develop equilibrium stresses. Such a domain length has a flow-through time of $\Delta_{ft} = 8\pi\delta_0/U_0$ or approximately 5000 time steps.

An example of the inflow Reynolds shear stress (the time and spanwise average of the covariance) obtained by applying (2.1) (with the first chosen set of random numbers) at the inflow is shown in figure 1(a). All target profiles are taken from a Spalart–Allmaras RANS simulation with the correction proposed by Coleman, Rumsey & Spalart (2018). The RANS simulation domain matched the DNS domain with an extension upstream to include a uniform flow stagnating upon a sharp leading edge from which the boundary layer develops. The RANS profiles were extracted at the DNS inflow location. In figure 1(a–d), the dash-dotted curve is a plot of the target shear stress profile. The dashed curve is the
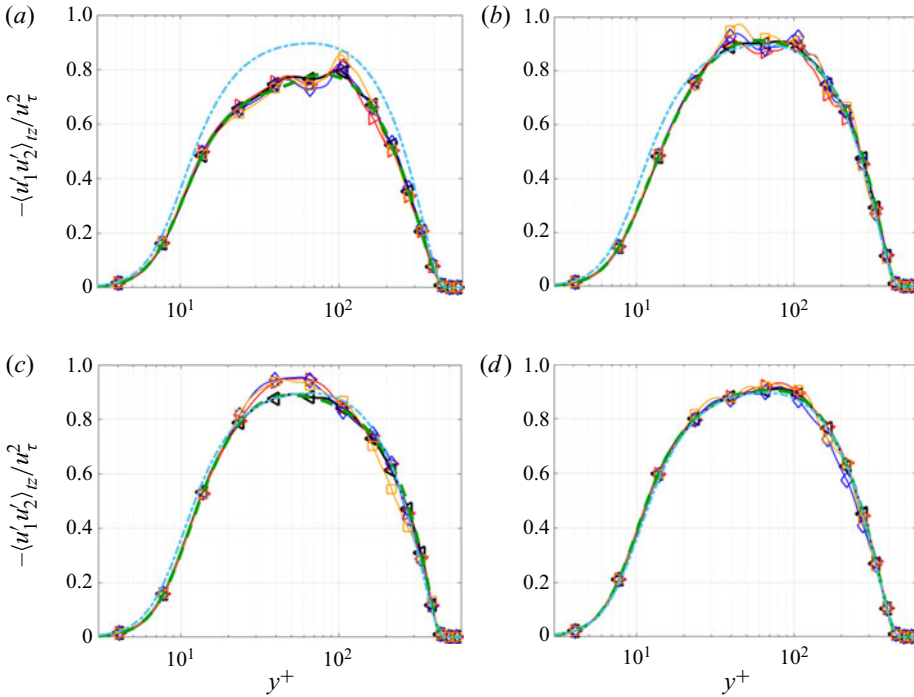
FIGURE 1. Reynolds shear stress $-R_{12}/u_\tau^2$ versus wall plus units: (*a*) typical random number set; (*b*) improved bias random number set; (*c*) σ-first sequential choice random number set; and (*d*) 'intelligent' design number set. Stress profile lines: dash-dotted, target; dashed, bias; solid, time convergence. Time level labelled with symbols: □, $1\Delta_{ft}$; ◇, $2\Delta_{ft}$; ▷, $4\Delta_{ft}$; and ◁, $20\Delta_{ft}$.

bias solution obtained by substituting (3.8) into (3.4) and further into (3.1), which displays how far off the target a first chosen random number set can be. The remaining curves of figure 1(*a*) display the span-time convergence at $t = 1, 2, 4$ and 20 times Δ_{ft}. The random number set in figure 1(*a*) was not fabricated to illustrate poor bias; rather, it was one from a real simulation whose poor performance was finally attributed to this unexpectedly poor random number set after a substantial time integration. This random number set demonstrates the bias and temporal convergence of typically sampled sets.

Applying only the bias improvement (e.g. keeping the d_i^n vectors from those of figure 1(*a*), but considering a large collection of random number sets and choosing the one with low bias error according to the first equation in (3.14*a,b*)) results in figure 1(*b*). Applying σ-first sequential choosing is shown in figure 1(*c*). Note that the bias error is further improved in figure 1(*c*) relative to figure 1(*b*) due to the greater freedom of having two random numbers (θ^n and ϕ^n) where figure 1(*b*) only had one (η^n) due to d_j^n being constrained to match figure 1(*a*). Figure 1(*d*) illustrates the results obtained with 'intelligent design'. A different seed was used and thus the bias results are similar but not the same as figure 1(*c*) (showing the run-to-run variation in bias with a σ-first approach). Note the span-time average is also improved with figure 1(*d*) showing the least variation of the four cases.

The plots of figure 1 are not only time but also spanwise averaged, which, through the action of $\widehat{\psi^n}$ can be seen in (3.7) to attenuate the time variation as the number of spanwise
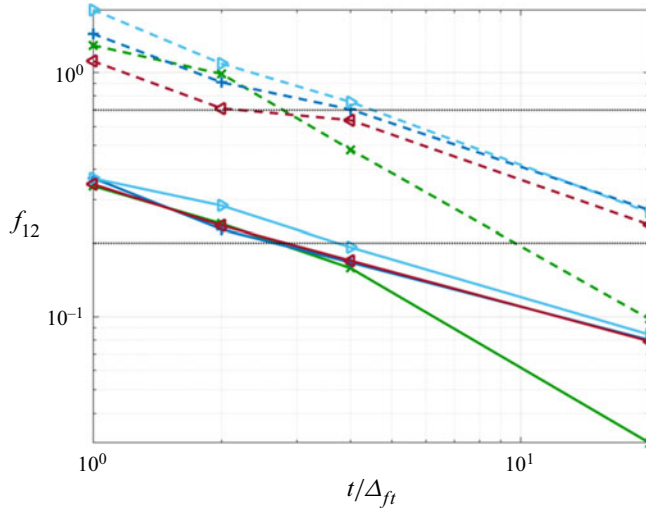
FIGURE 2. Time convergence of spanwise variation of stress fluctuations as a function of flow-through times: f_{12}^{max} (dashed); f_{12}^{rmy} (solid). Symbols: +, figure 1(*a*); ▷, figure 1(*b*); ◁, figure 1(*c*); ×, figure 1(*d*); · · · · · ·, DNS channel.

samples increases (average of sine is zero). Figure 1 is presented with spanwise averaging because it is the common way that researchers assess time convergence, exploiting the spatial homogeneity. However, a more clear view of the temporal convergence can be obtained by considering the normalized spanwise-varying stress fluctuation $f_{ij} = \langle u_i'^{+} u_j'^{+} \rangle_t (y, z) - \langle u_i'^{+} u_j'^{+} \rangle_{tz}(y)$, which decays as $\lim_{t\to\infty} f_{ij} = 0$ without mixing in spatial averaging.

The variation of f_{ij} with Δ_{ft} is plotted two ways in figure 2 for each of the four cases considered in figure 1. The dashed lines show $f_{ij}^{max} = \max_y(\max_z(f_{ij}))$, which can be thought of as the largest local stress deviation from its spanwise average for a given interval's time average (e.g. error of the poorest converged stress across the entire inflow plane). The solid line shows $f_{ij}^{rmy} = \max_y(f_{ij}^{rms})$, which can be thought of as the least time-converged r.m.s. variation of f_{ij}.

As this is a somewhat non-traditional quantity, the channel flow DNS database of (Graham *et al.* 2016) was used to assess the expected level of f_{12}^{max} and f_{12}^{rmy} after one channel flow-through time. This channel flow database was chosen over flat-plate data because of the lack of inflow boundary condition assumptions. The Re_τ for both cases are similar – this paper's flat plate ranges from $Re_\tau = 600$–1000 while the channel $Re_\tau = 1000$. Mining the entire time-continuous segment of the database (one channel flow-through time) at five wall-normal locations and 10 streamwise locations yielded values of $f_{12}^{max} \approx 0.7$ and $f_{12}^{rmy} \approx 0.2$, which are added to figure 2 as dotted lines. Comparing the dashed curves, none of the curves meets the channel value of f_{12}^{max} at $2\Delta_{ft}$ though most have by $4\Delta_{ft}$. Likewise, comparing the solid curves, all four cases are close to f_{12}^{rmy} of the channel after $2\Delta_{ft}$ but only the 'intelligent design' case exhibits the expected asymptotic $1/t$ convergence after $4\Delta_{ft}$ as it also did for f_{12}^{max}. It must be noted that the Reynolds number and flow (channel versus boundary layer) differences likely render the dotted lines as rough targets/guidelines for temporal convergence measures.
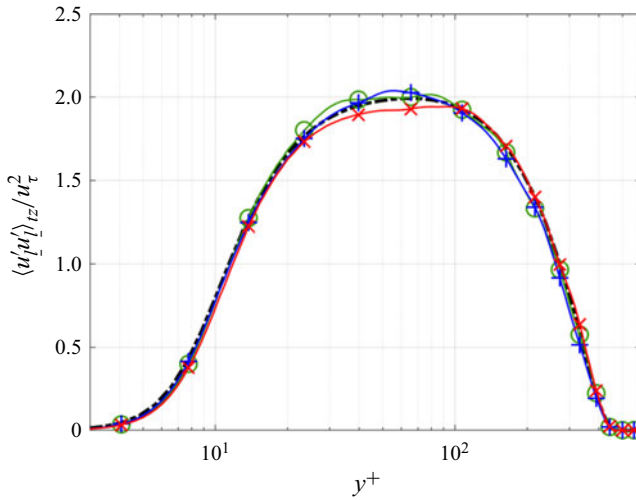
906 R1-10

FIGURE 3. Normal Reynolds stress profile with 'intelligent design' random number set at $2\Delta_{ft}$. Symbols: - - - -, R_{iso}; $\circ$, R_{11}; $+$, R_{22}; $\times$, R_{33}.

Though not shown here, the choice of ψ^n influences early-time convergence through the numerator of (3.7), but, as most scale-resolving simulations integrate over multiple Δ_{ft}, the improved convergence in the $t \geq 4\Delta_{ft}$ range from 'intelligent design' is significant. Note that figure 2 shows that the time convergence of the case in figure 1(*c*) is as good as or better than the cases in figure 1(*a*) and figure 1(*b*). This contradicts the visual results in figure 1 confirming the muddled view of time convergence introduced by spanwise averaging in figure 1.

While the prediction of the shear stress at the inflow is the most important stress, the normal stresses are also important in some applications. Figure 3 shows that the mode set that created figure 1(*d*) ('intelligent design') resulted in excellent biases for the normal stresses as well. Note that all three target stresses were set to isotropic values consistent with information available from a one- or two-equation RANS closure. To achieve this result, in (3.14*a,b*), $w_{12} = w_{21} = 25$, $w_{22} = 5$ and all other $w_{ij} = 1$. Equal weights for all components yielded relatively larger bias error (not shown) in R_{12} as noted in (3.16).

Direct numerical simulations with two different random number sets were performed, and the evolution of the wall coefficient of friction C_f is shown in figure 4. The high-bias random number simulation requires a substantially longer development length to reach the 5 % margin from Smits *et al.* (1983) correlation, which at this Reynolds number is in good agreement with Coles's (1962) experiment and Jimenez *et al.*'s (2010) DNS. The low-bias inflow reaches the 5 % margin within two to three boundary layer thicknesses as opposed to six for the high bias. Both eventually come to better agreement in eight and 10 boundary layer thicknesses, respectively. Better agreement in the early region offers significant advantage when applied to flows with pressure gradients whose development is not as forgiving as the zero-pressure-gradient cases presented here.

It is important to mention that the spike in wall shear immediately downstream of the inflow is to be expected with this STG method (Shur *et al.* 2014), and is caused by the near-wall synthetic turbulence developing the correct physics (e.g. wall streaks). As a consequence, this spike is larger with DNS (see also the simulations of Spalart *et al.* (2017)) than with other methods that do not fully resolve the near-wall turbulence,
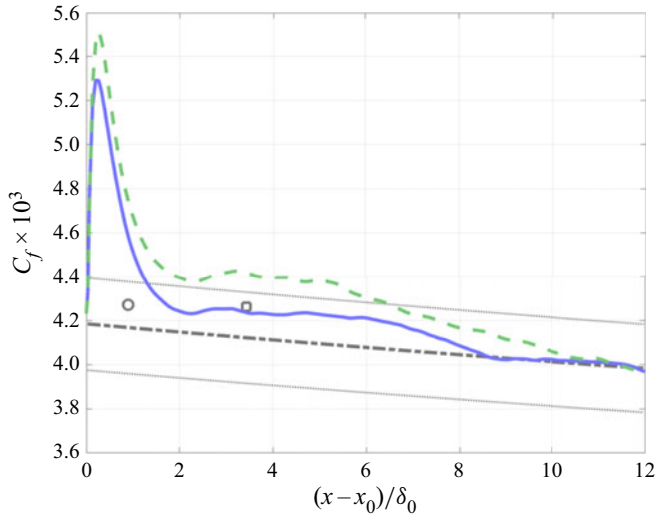
FIGURE 4. Coefficient of friction versus development length for high-bias (dashed) and low-bias (solid) inflow; Smits, Matheson & Joubert (1983) correlation (dash-dotted) with 5 % variation (dotted); Coles (1962) experiment, □ ; and Jimenez *et al.* (2010) DNS, ○.

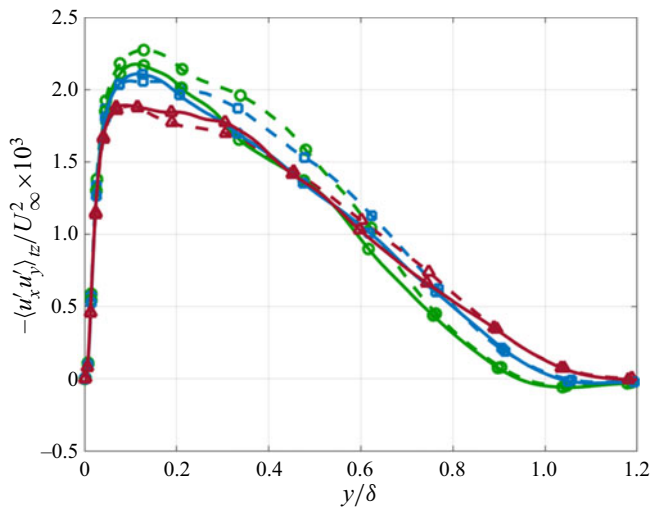FIGURE 5. Reynolds shear stress profiles for high (dash) and low (solid) inflow bias at 3 (○), 5 (□) and 10 (△) boundary layer thicknesses downstream of inflow.

such as the hybrid RANS/LES model used in Shur *et al.* (2014) and figure 6. The shear stress profiles shown in figure 5 illustrate the same delayed convergence of the high-bias inflow relative to the low-bias inflow. At $3\delta_0$ downstream the high-bias stress profile has a substantial bulge in the range of $0.1 < y/\delta_0 < 0.6$, which decreases in both magnitude and range, $0.25 < y/\delta_0 < 0.6$ by $5\delta_0$, and is virtually eliminated by $10\delta_0$.

As additional verification of the correctness of the implementation of Shur *et al.*'s (2014) method, we repeat one simulation performed therein – a wall-modelled LES of fully developed turbulent flow in a channel. In order to allow direct comparisons to the
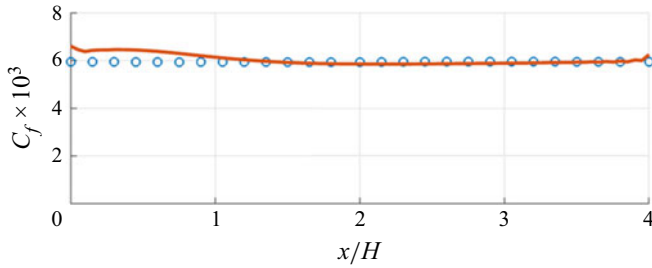
FIGURE 6. Coefficient of friction as a function of development length for a wall-modelled LES of a channel utilizing STG (solid line) compared to periodic boundary conditions (○).
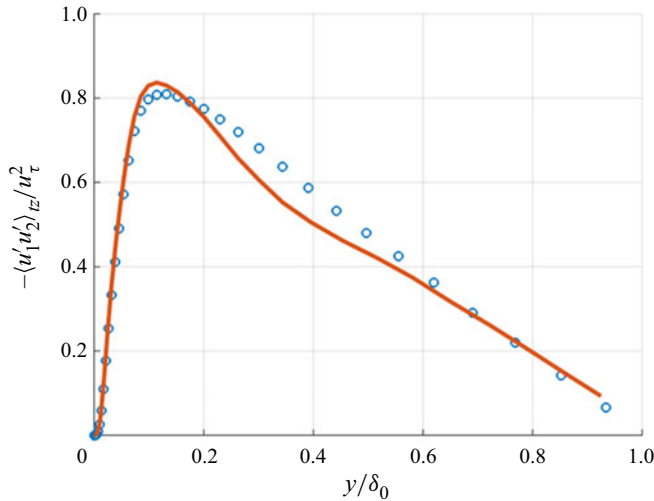

FIGURE 7. Reynolds shear stress profile six boundary layer thicknesses downstream of STG inflow (solid line) compared to results obtained with periodic boundary conditions (○), both using wall-modelled LES.

original results of the method, the problem set-up matched those described in Shur *et al.* (2014). The Reynolds number based on the half-height is $Re_\tau = 400$, the grid has spacing $\Delta x^+ = 40$, $\Delta z^+ = 20$, $\Delta y^+_{min} = 0.8$ and $\Delta y_{max} = 0.04H$, where H is the channel height. The turbulence model used was IDDES (improved delayed detached-eddy simulation) (Shur *et al.* 2008) based on the Spalart–Allmaras RANS closure (Spalart & Allmaras 1994). Figure 6 shows that, for this channel flow, similarly to the flat-plate boundary layer, with the STG inflow boundary condition the skin friction is recovered within 3δ ($\delta = H/2$) and the Reynolds shear stress agrees well with the solution obtained with periodic boundary conditions at 6δ as shown in figure 7. These results are consistent with the ones obtained by Shur *et al.* (2014) for the IDDES-SST (shear stress transport) k–ω model.

It is important to highlight that the analysis of the errors and the choosing of the random variables that are the focus of this paper are completely independent of the specific flow problem. Of course, the target mean velocity and stress profiles will change; however, the process of minimizing bias and obtaining adequate time convergence of the statistics

does not (with the exception of the selection of the weights in (3.14*a,b*), which should be tailored to prioritize the most important stress components).

5. Conclusions

Two types of STG error, bias and temporal convergence, were identified and explicit predictions for the value of those errors were developed in terms of the simulation parameters (e.g. mesh sizes on application plane, mean stress profiles, N) and, more importantly, the four random numbers for the angles associated with each of the N modes. These predictions provided a means to select random numbers that minimized each of the errors separately. Data from the inflow plane of an ongoing DNS were used to demonstrate the impact of STG under certain poor random number sets and, more importantly, to verify that the aforementioned error measures could be used to identify random number sets with very low bias and better STG performance. The time convergence was verified to be similar to that of stresses on the interior of the domain when the temporal error term was taken into account. Both error measures provide a means to quantify and minimize inflow differences in simulations that are intended to be compared to other simulations, which will hopefully allow a more direct comparison of the interior modelling and discretization.

Note that the above analysis is currently limited to the class of STG methods that uses a fixed set of random numbers for the full time of the simulation, but extensions to methods that allow time-varying random numbers (Xie & Castro 2008) will be considered in future work. The error analysis provided in this paper is limited to cases where the boundary condition is enforced strongly (Dirichlet) and directly to velocity components. The effect of weak (Neumann) enforcement or nonlinear boundary conditions, which are important to many numerical methods, will also be considered in future work.

Acknowledgements

Declaration of interests

The authors report no conflict of interest.

References

ADAMIAN, D. Y., STRELETS, M. K. & TRAVIN, A. K. 2011 An efficient method of synthetic turbulence generation at LES inflow in zonal RANS-LES approaches to computation of turbulent flows. *Math. Mod.* **23**, 3–19.

BALIN, R., JANSEN, K. E. & SPALART, P. R. 2020 Wall-modeled LES of flow over a Gaussian bump with strong pressure gradients and separation. In *AIAA AVIATION Forum*, 3012.

BATTEN, P., GOLDBERG, U. & CHAKRAVARTHY, S. 2004 Interfacing statistical turbulence closures with large-eddy simulation. *AIAA J.* **42**, 485–482.

BÉCHARA, W. 1994 Stochastic approach to noise modeling for free turbulent flows. *AIAA J.* **32**, 455–463.

COLEMAN, G. N., RUMSEY, C. L. & SPALART, P. R. 2018 Numerical study of turbulent separation bubbles with varying pressure gradient and Reynolds number. *J. Fluid Mech.* **847**, 28–70.

COLES, D. E. 1962 The turbulent boundary layer in a compressible fluid. *Tech. Rep.* R-403-PR. The Rand Corporation.

GRAHAM, J., KANOV, K., YANG, X. I. A., LEE, M. K., MALAYA, N., LALESCU, C. C., BURNS, R., EYINK, G., SZALAY, A., MOSER, R. D. *et al.* 2016 A web services-accessible database of turbulent channel flow and its use for testing a new integral wall model for LES. *J. Turbul.* **17** (2), 181–215.

HUANG, S. H., LI, Q. S. & WU, J. R. 2010 A general inflow turbulence generator for large eddy simulation. *J. Wind Engng Ind. Aerodyn.* **98**, 600–617.

JIMENEZ, J., HOYAS, S., SIMENS, M. P. & MIZUNO, Y. 2010 Turbulent boundary layers and channels at moderate Reynolds numbers. *J. Fluid Mech.* **657**, 335–360.

KARWEIT, M., BLANC-BENON, PH., JUVÉ, B. & COMTE-BELLOT, G. 1991 Simulation of the propagation of an acoustic wave through a turbulent velocity field: a study of phase variance. *J. Acoust. Soc. Am.* **89**, 52–62.

KRAICHNAN, R. H. 1970 Diffusion by a random velocity field. *Phys. Fluids* **12**, 22–31.

LUND, T. S., WU, X. & SQUIRES, K. D. 1998 Generation of turbulent inflow data for spatially-developing boundary layer simulations. *J. Comput. Phys.* **140**, 233–258.

SHUR, M. L., SPALART, P. R., STRELETS, M. K. & TRAVIN, A. K. 2008 A hybrid RANS-LES approach with delayed-DES and wall-modelled LES capabilities. *Intl J. Heat Fluid Flow* **29**, 1638–1649.

SHUR, M. L., SPALART, P. R., STRELETS, M. K. & TRAVIN, A. K. 2014 Synthetic turbulence generators for RANS-LES interfaces in zonal simulations of aerodynamic and aeroacoustic problems. *Flow Turbul. Combust.* **93**, 63–92.

SMIRNOV, A., SHI, S. & CELIK, I. 2001 Random flow generation technique for large eddy simulations and particle-dynamics modeling. *Trans. ASME: J. Fluids Engng* **123**, 359–371.

SMITS, A. J., MATHESON, N. & JOUBERT, P. N. 1983 Low-Reynolds-number turbulent boundary layers in zero and favorable pressure gradients. *J. Ship Res.* **27**, 147–157.

SPALART, P. R. & ALLMARAS, S. R. 1994 A one-equation turbulence model for aerodynamic flows. *Recherche Aerospatiale* **1**, 5–21.

SPALART, P. R., BELYAEV, K. V., GARBARUK, A. V., SHUR, M. L., STRELETS, M. K. & TRAVIN, A. K. 2017 Large-eddy and direct numerical simulations of the Bachalo-Johnson flow with shock-induced separation. *Flow Turbul. Combust.* **99**, 865–885.

SPILLE-KOHOFF, A. & KALTENBACH, H. J. 2001 Generation of turbulent inflow data with a prescribed shear-stress profile. In *Proceedings of the Third AFOSR International Conference on DNS/LES* (ed. C. Liu, L. Sakell & T. Beutner). Texas University at Arlington.

WU, X. 2017 Inflow turbulence generation methods. *Annu. Rev. Fluid Mech.* **49**, 23–49.

XIE, Z. T. & CASTRO, I. P. 2008 Efficient generation of inflow conditions for large eddy simulation of street-scale flows. *Flow Turbul. Combust.* **81**, 449–470.